NASA Technical Memorandum 107732

WING FLUTTER BOUNDARY PREDICTION USING AN UNSTEADY EULER AERODYNAMIC METHOD

ELIZABETH M. LEE-RAUSCH
JOHN T. BATINA

MARCH 1993

National Aeronautics and Space Administration

Langley Research Center
Hampton, Virginia 23681-0001

WING FLUTTER BOUNDARY PREDICTION USING UNSTEADY EULER AERODYNAMIC METHOD

Elizabeth M. Lee-Rausch*
John T. Batina**
NASA Langley Research Center
Hampton, Virginia 23681–0001

Abstract

Modifications to an existing three-dimensional, implicit, upwind Euler/Navier-Stokes code (CFL3D Version 2.1) for the aeroelastic analysis of wings are described. These modifications, which were previously added to CFL3D Version 1.0, include the incorporation of a deforming mesh algorithm and the addition of the structural equations of motion for their simultaneous time-integration with the governing flow equations. The paper gives a brief description of these modifications and presents unsteady calculations which check the modifications to the code. Euler flutter results for an isolated 45° swept-back wing are compared with experimental data for seven freestream Mach numbers which define the flutter boundary over a range of Mach number from 0.499 to 1.14. These comparisons show good agreement in flutter characteristics for freestream Mach numbers below unity. For freestream Mach numbers above unity, the computed aeroelastic results predict a premature rise in the flutter boundary as compared with the experimental boundary. Steady and unsteady contours of surface Mach number and pressure are included to illustrate the basic flow characteristics of the time-marching flutter calculations and to aid in identifying possible causes for the premature rise in the computational flutter boundary.

Nomenclature

A_{ij}	generalized aerodynamic force resulting from pressure induced by mode j acting through mode i
b	root semichord
c	root chord
c_i	generalized damping of mode i
C_p	pressure coefficient
k	reduced frequency, $\frac{\omega c}{2U_\infty}$
k_i	generalized stiffness of mode i
$\hat{m}$	measured wing panel mass
m_i	generalized mass of mode i
M_∞	freestream Mach number
q_i	generalized displacement of mode i
Q_i	generalized force of mode i
T	dimensional time
u_i	load vector
U_F	flutter speed
U_∞	streamwise freestream speed
v	volume of a truncated cone having streamwise root chord as lower base diameter, streamwise tip as upper base diameter, and panel span as height
x_i	state vector
α	steady-state angle of attack
Θ	integral of the state-transition matrix
μ	mass ratio, $\frac{\hat{m}}{\rho v}$
σ_j	damping associated with mode j of the aeroelastic response
Φ	state-transition matrix
ω	angular frequency
ω_j	frequency associated with mode j of the aeroelastic response
ω_α	uncoupled natural frequency of the wing first torsion mode

Introduction

Research during the last decade on the application of computational fluid dynamics (CFD) methods to unsteady flows and aeroelastic analysis has been rapidly progressing. Edwards and Malone[1] recently presented a survey on the status of computational methods for unsteady aerodynamic and aeroelastic analysis with an emphasis on methods for transonic flows. The transonic speed range has been a main focus of activity because flutter dynamic pressures are typ-

*Research Engineer, Unsteady Aerodynamics Branch, Structural Dynamics Division. Member AIAA.

**Senior Research Scientist, Unsteady Aerodynamics Branch, Structural Dynamics Division. Associate Fellow AIAA, Member ASME.

ically critical (lower) in this speed range. Much of this research, especially for three-dimensional configurations, has focused on the development of finite-difference methods for the solution of the transonic small disturbance (TSD) and full potential (FP) equations.[1] One reason for the focus on the FP and TSD methods is that the reduced memory and run-time requirements of these methods in comparison with the higher-order methods have made them more viable for use in aeroelastic analyses of three-dimensional configurations. Edwards and Malone[1] reported on 13 aeroelastic studies of flexible wings and flexible wings/rigid body configurations which utilized the TSD and FP methods. These studies, which compare flutter boundary calculations with experimental data, provide important applications of these CFD methods.

Reference 1 points out that many critical challenges facing computational aeroelaticity will require the modeling of increasingly more complex flow physics. To meet these challenges, researchers have begun to develop higher-order methods involving the Euler and Navier/Stokes equations for unsteady aerodynamic and aeroelastic analysis. With recent advances in algorithm development and computer hardware, higher-order methods utilizing the Euler and Navier/Stokes equations have been used in three-dimensional aeroelastic applications;[2–11] however, the number of these applications lags behind those utilizing the TSD and FP methods largely in part because of their increased computational requirements.

The research described in Refs. 2–11 represents important steps in the development of three-dimensional Euler and Navier/Stokes methods for aeroelastic analysis. However, continuing studies are needed to validate these methods for the prediction of aeroelastic response and flutter. In Ref. 3, Robinson et al. performed time-marching flutter calculations for an isolated 45° swept-back wing using an Euler code. A novel aspect of the capability described in Ref. 3 was the deforming mesh algorithm which was used to move the mesh so that it conformed continuously to the instantaneous position of the wing. The results presented compared favorably with the experimental data and with results from a transonic small disturbance code for the single flutter point analyzed. The purpose of the present work is to further demonstrate and assess the capability presented in Ref. 3 by completing the flutter boundary for the simple, well-defined, isolated 45° swept-back wing configuration using the Euler equations. The wing analyzed in these studies is the first AGARD standard aeroelastic configuration for dynamic response, and its flutter data is an accepted set with which to test codes.[12] In Ref. 3, modifications were made to an existing three-dimensional, unsteady Euler/Navier-Stokes code (CFL3D Version 1.0) for the aeroelastic analysis of wings. These modifications included the incorporation of a deforming mesh algorithm and the addition of the structural equations of motion for their simultaneous time-integration with the governing flow equations. The deforming mesh algorithm and the structural equations of motion described in Ref. 3 have been added to the most recently released version of CFL3D, Version 2.1, by the present authors. This paper gives a brief description of these modifications and presents unsteady calculations which check the modifications to the code. Results from calculations performed for a rigid wing undergoing forced pitching and plunging motions are presented to test the performance of the deforming mesh algorithm. Aeroelastic results for the 45° swept-back wing at a freestream Mach number of 0.9 are compared to those presented in Ref. 3 to check the addition of the structural equations of motion. Calculated flutter results for the same 45° swept-back wing are compared with the experimental data for seven freestream Mach numbers which define the flutter boundary over a range of Mach number from 0.499 to 1.14. Steady-state Mach contours of the initial flowfields are also included in the discussion of the aeroelastic results to illustrate the basic flow characteristics of the time-marching flutter calculations at selected freestream Mach numbers. Instantaneous surface pressure contours during an aeroelastic transient at $M_\infty = 0.99$ are presented to demonstrate changes in the flowfield which are induced by the aeroelastic motions.

Upwind Euler/Navier-Stokes Algorithm

The time-dependent Euler equations are solved within the CFL3D[13, 14] code by a three-factor, implicit, finite-volume algorithm based on upwind-biased spatial differencing. The algorithm, which is a cell-centered scheme, uses upwind differencing based on either flux-vector splitting or flux-difference splitting. Both types of upwind differencing account for the local wave-propagation characteristics of the flow and sharply capture shock waves. Also, because these schemes are naturally dissipative, additional artificial dissipation terms are not necessary. Several types of flux-limiting are available within the code to prevent oscillations in the solution near shock waves. These oscillations are typically found in results from higher-order schemes. For unsteady cases, the original algorithm contains the necessary metric terms for a rigidly translating and rotating mesh which moves without deforming. For cases involving a deforming mesh, however, an additional term accounting for the change in cell volume must be included in the time-discretization of the governing equations. This modification is implemented as described in Ref. 3. The aeroelastic equations of motion were implemented in the more recent Version 2.1 because, in addition to other improvements, this code contains several options for computing multi-block solutions which will be utilized in future computations.

Deforming Mesh Algorithm

In the time-marching aeroelastic calculations, the mesh must be updated at every time level so that it conforms to the aeroelastically deformed shape of the wing. Because the

aeroelastic motion of the wing may be general in nature and are not known a priori, a general mesh updating procedure is necessary. One such method, the deforming mesh algorithm, models the mesh as a network of springs and solves the static equilibrium equations for this network to determine the new locations of the mesh grid points. This algorithm was originally developed by Batina[15] for tetrahedral cells and extended by Robinson et al.[3] for hexahedral cells. The edge of each hexahedral cell is modeled as a spring whose stiffness is inversely proportional to the length of the edge raised to a power. In order to control cell shearing and to prevent the collapse of the cell, diagonal springs are added along the faces of each cell. Similarly, the stiffness of the diagonal springs is also inversely proportional to the length of the diagonal raised to a power. As suggested in Ref. 3, a power of three was used in the present calculations.

At each time level, the grid points on the outer boundary are held fixed, and the displacement of the wing surface is specified. For aeroelastic calculations, the displacement is determined from the integration of the structural equations of motions. The new locations of the interior grid points are then determined by solving the static equilibrium equations which result from a summation of forces in the x, y and z coordinate directions at each grid point. These static equilibrium equations are solved using a predictor-corrector method. The new grid point locations are first predicted by an extrapolation from the previous two time levels and then corrected by using several Jacobi iterations of the static equilibrium equations. In the present calculations, four Jacobi iterations are sufficient to move the mesh.

Although the deforming mesh algorithm is a general procedure, the current implementation in CFL3D is restricted to meshes of C-H topology. This limitation is due to the specialized treatment required for the mesh boundaries. For example, in a C-H mesh the plane of points represented by the maximum i index would be an outer boundary; however, in a C-O mesh the plane of points represented by the maximum i index would be an internal cut.

Time-Marching Aeroelastic Analysis

In a time-marching aeroelastic analysis, the calculation of each flutter point is begun by obtaining a static aeroelastic solution about the wing. There are several ways to obtain a static aeroelastic solution. One way is to compute a steady-state solution about the rigid wing. The next step is to allow the rigid wing to deform to the steady loads until a static aeroelastic solution is obtained. The calculation of the static deformation is obtained using the aeroelastic equations of motion. For this time-marching calculation, however, the structural damping of the wing is set to a number, around 0.99, such that the dynamic system is near critically damped. The aeroelastic equations of motion are then marched simultaneously in time with the governing flow equations until the wing no longer deforms under the aerodynamic loads. Since the system is very damped, this calculation does not require a great amount of computational time. The static aeroelastic solution is then used as the starting point for the time-marching dynamic aeroelastic solution. Since the wing analyzed in the present work has a symmetric airfoil section, at zero degree angle of attack this configuration will have no static deflection. Therefore, for this wing, the steady, rigid solutions could be used as the starting solutions for the aeroelastic time-marching calculations.

In order to bracket the flutter point, the static aeroelastic and dynamic aeroelastic computations are computed at several values of dynamic pressure (typically three values) which ranged from 80% to 120% of the experimental values depending on the freestream Mach number. In each of the dynamic aeroelastic calculations, the motion of the wing is initiated by specifying a small initial velocity for the first two modes. The resulting transients are analyzed with a modal identification technique for their damping and frequency content. The computed flutter dynamic pressure and frequency can then be determined by interpolating the specified dynamic pressures and the computed frequencies to the zero damping value of the dominant mode at flutter. The subsequent sections contain a brief description of the aeroelastic equations of motion, the time-marching solution procedure, and the modal identification technique.

Aeroelastic Equations of Motion

The aeroelastic equations of motion that are incorporated within CFL3D are similar to those described in Refs. 3 and 16. In this formulation, the equations are derived by assuming that the general motion of the wing can be described by a separation of time and space variables in a finite modal series. This modal series consists of the summation of the free vibration modes weighted by the generalized displacements. After applying Lagrange's equations to this system, the aeroelastic equations of motion can then be written for each vibration mode i as

$$m_i\ddot{q}_i + c_i\dot{q}_i + k_i q_i = Q_i \tag{1}$$

where q_i is the generalized displacement, m_i is the generalized mass, c_i is the generalized damping, k_i is the generalized stiffness, and Q_i is the generalized aerodynamic force computed by integrating the pressure weighted by the mode shapes. The superscript dots in Eq. (1) represent differentiation with respect to time.

Time-Marching Solution

The solution procedure implemented in CFL3D for integrating Eq. (1) is that described by Edwards et al.[17, 18] The linear state equations are written as

$$\dot{x}_i = Ax_i + Bu_i \tag{2}$$

where A and B are coefficient matrices that result from the change of variables $x_i = [q_i\ \dot{q}_i]^T$ and u_i is the nondimensional representation of the generalized force Q_i. Equation (2) is integrated in time using the modified state-transition matrix structural integrator[17] implemented as a predictor-corrector procedure. The prediction for x_i^{n+1}, $\tilde{x}_i^{n+1}$, is given by

$$\tilde{x}_i^{n+1} = \Phi x_i^n + \Theta B\left(3u_i^n - u_i^{n-1}\right)/2 \qquad (3)$$

where Φ is the state-transition matrix and Θ is the integral of the state-transition matrix from time step n to $n+1$. The predicted value of the generalized displacement $\tilde{x}_i^{n+1}$ is used to update the mesh for the next flow field calculation which is used in turn to evaluate the nondimensional generalized force $\tilde{u}_i^{n+1}$. These values are then used in the corrector step to determine x_i^{n+1}, given by

$$x_i^{n+1} = \Phi x_i^n + \Theta B\left(\tilde{u}_i^{n+1} + u_i^n\right)/2 \qquad (4)$$

Modal Identification Technique

Damping and frequency characteristics of the aeroelastic responses are estimated from the response curves by using the modal identification technique of Bennett and Desmarais.[19] The modal estimates are determined by a least squares curve fit of the responses of the form

$$q_i(T) = a_o + \sum_{j=1}^{m} e^{\sigma_j T}\left[a_j cos(\omega_j T) + b_j sin(\omega_j T)\right] \qquad (5)$$
$$i = 1, 2, 3, \ldots$$

where q_i is the generalized displacement of the natural vibration mode i (as previously defined) and where σ_j and ω_j are the damping and frequency, respectively, associated with mode j of the aeroelastic response. The number of modes m determined in the curve fit of the response is usually greater than or equal to the number of modes initially excited.

Pulse Transfer-Function Analysis

Generalized aerodynamic forces (GAF's) can be obtained by calculating several cycles of a forced harmonic oscillation and using the last cycle of oscillation to determine the load. This requires one time-marching calculation for each value of reduced frequency and each mode of interest. In contrast, the GAF's may be determined for a wide range of reduced frequency in a single time-marching calculation for each mode using the pulse transfer-function analysis. In the pulse analysis, the unsteady force is computed indirectly from the response of the flowfield due to a wing motion that is represented by a smoothly varying, exponentially shaped pulse. A fast Fourier transform of the unsteady force is divided by the Fourier transform of the displacement to obtain the GAF. The pulse transfer-function analysis has been previously employed to determine the GAF's which are used in aeroelastic analyses.[3, 16, 20–22] Results presented in Refs. 3, 16 and 20–22 have shown that the analysis is valid for predicting the small perturbation response about a nonlinear flowfield.

Wind Tunnel Model Description

The wing being analyzed in this study is the first AGARD standard aeroelastic configuration for dynamic response, Wing 445.6,[12] which was tested in the Transonic Dynamics Tunnel (TDT) at NASA Langley Research Center.[23] The Wing 445.6 has a quarter-chord sweep angle of 45°, a panel aspect ratio of 1.65, a taper ratio of 0.66, and a NACA 65A004 airfoil section. A planform view of this wing is shown in Fig. 1. Several different models of the Wing 445.6 were tested in the TDT including both full span and semi-span models. The model used in this study was one of the semi-span wind tunnel-wall-mounted models which was constructed of laminated mahogany. In order to obtain flutter data for a wide range of Mach number and density conditions in the TDT, holes were drilled through several of the mahogany wings to reduce their stiffness. The aerodynamic shape of the original wing was preserved by filling the holes with rigid foam plastic. A photograph of a weakened model mounted in the TDT is shown in Fig. 2. The model designated as "WEAK3" in Ref. 23 is analyzed herein. The flutter data for this model tested in air is reported in Ref. 23 over a range of Mach number from 0.499 to 1.141.

The Wing 445.6 is modeled structurally using the first four natural vibration modes which are illustrated in Figs. 3(a) and (b). Figure 3(a) shows oblique projections of the natural modes while Fig. 3(b) shows the corresponding deflection contours. These modes which are numbered 1 through 4 represent first bending, first torsion, second bending, and second torsion, respectively, as calculated by a finite element analysis.[23] The modes have natural frequencies which range from 9.6 Hz for the first bending mode to 91.54 Hz for the second torsion mode. As suggested in Ref. 23, the experimentally determined modal frequencies were used in the time-marching flutter analysis. For the cases considered in this study, no structural damping is included in the aeroelastic equations of motion ($c_i = 0$ for all modes).

Results and Discussion

Results are presented in this section for calculations about the Wing 445.6. All of the computational results were obtained using a 193 x 33 x 41 C-H-type grid with 193 points wrapped around the wing and its wake (129 points on the wing surface), 41 points distributed from the wing root to the spanwise boundary (25 points on the wing surface), and 33 points distributed radially from the wing surface to the outer boundary. This mesh topology was chosen rather

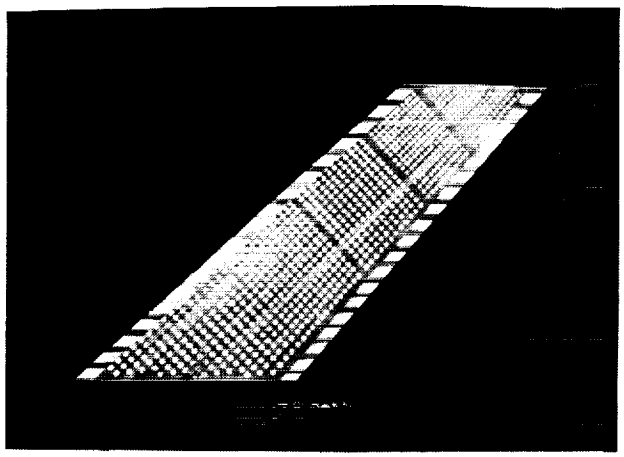

Figure 1 Planform view of Wing 445.6.

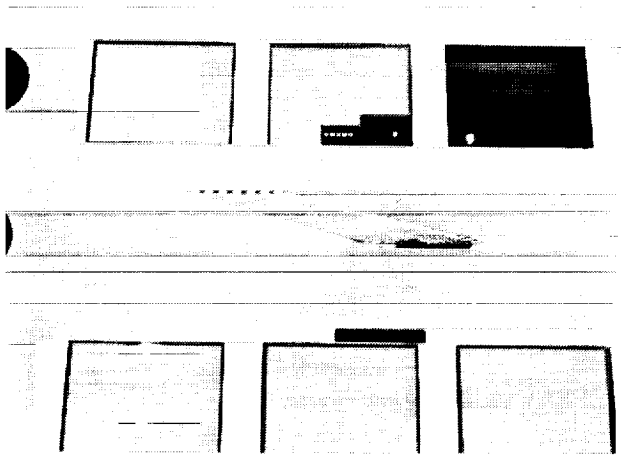

Figure 2 Wing 445.6 model in the NASA Langley Transonic Dynamics Tunnel.

than a C-O-type topology because the wind tunnel model has a sheared-off tip. This can be seen in the photograph of the model in Fig. 2. A partial view of the surface mesh on the wing and symmetry plane is shown in Fig. 4. Its outer boundaries extend 10 local chord lengths to the upstream and downstream boundaries, 10 local chord lengths to the upper and lower boundaries, and 1 semi-span length off of the tip. Note that this grid is identical to the one used in Ref. 3.

For all of the calculations, the Euler equations are solved using flux-vector splitting and a smooth flux-limiter. Convergence to steady-state was accelerated using local time-stepping, mesh sequencing and multi-grid cycling. For time-marching calculations, the nondimensional global time-step (based on the root chord and the freestream speed of sound) was 0.05456. The in-core memory requirement for this grid was 25 Mw on a Cray-2 computer which is 15.6 Mw over what is required for the unmodified CFL3D Version 2.1. Recent coding modifications have reduced the additional memory requirements for the aeroelastic version by approximately 50%, and so the current grid would now require 17.4 Mw. Each of the steady-state calculations required approximately 3–4 hours of CPU time on a Cray-2 computer to converge the solution to an acceptable level (6 orders of magnitude). Aeroelastic transients were computed at each dynamic pressure for approximately 2 cycles of the lowest frequency modal motion. These calculations typically required 8 hours of CPU time. Since aeroelastic transients were computed for three different values of dynamic pressure at each freestream Mach number, the total computational cost for each flutter point (including the steady-state solution) was approximately 28 hours of CPU time.

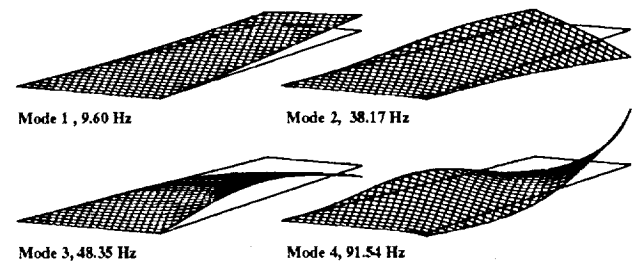

(a) oblique projections.

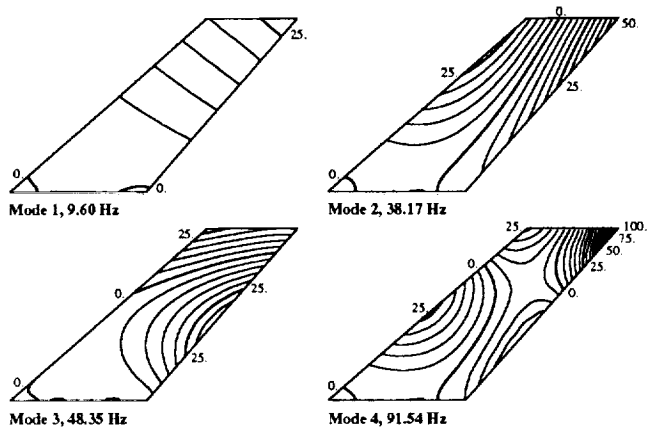

(b) deflection contours.

Figure 3 Natural vibrations modes for Wing 445.6.

Pulse Transfer-Function Results

The generalized forces for the Wing 445.6 at $M_\infty = 0.9$ were computed using the pulse transfer-function analysis method described in a preceding section. The pulse calculations were restarted from a steady-state flow condition at an angle of attack of $\alpha = 0°$. A plunging motion and a pitching motion about the root quarter chord, which are defined as modes h and θ respectively, were analyzed. These simple "modes" were chosen in order that the motion of the wing could be simulated not only by the deforming mesh algorithm but also by a rigid translation and rotation of the grid. The maximum amplitude of the plunging motion was 0.01 root chord lengths, and the maximum pitch amplitude was 1°. The results of the pulse analyses, shown in Fig. 5, are plotted in terms of the real and imaginary components of

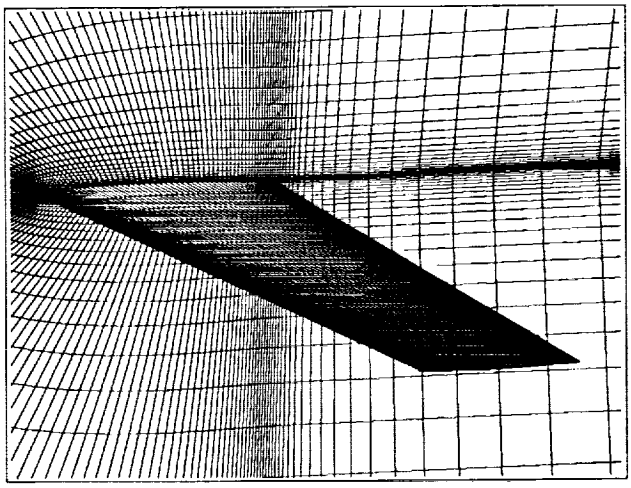

Figure 4 Partial view of the 193 x 33 x 41 computational grid on the wing surface and symmetry plane.

the unsteady forces as a function of the reduced frequency k which is defined by $\frac{\omega b}{U_\infty}$. The generalized force A_{hh} is the lift due to plunge, $A_{h\theta}$ is the lift coefficient due to pitching, $A_{\theta h}$ is the pitching moment due to plunge, and $A_{\theta\theta}$ is the pitching moment due to pitch. As shown in Fig. 5, the forces from the pulse analysis obtained using the deforming mesh agree very well with the forces obtained using the rigidly moving mesh. This good agreement between the results verifies the three-dimensional deforming mesh capability which was implemented in the code.

Flutter Results

Flutter characteristics were determined for seven freestream Mach numbers, M_∞ = 0.499, 0.678, 0.900, 0.960, 0.990, 1.072, and 1.141 at $\alpha = 0°$ angle of attack. Each time-marching calculation was restarted from the steady-state solution about the rigid wing, and the motion of the wing was initiated by specifying a small initial velocity for the first two modes. The resulting transients were analyzed for their damping and frequency content with the modal identification technique which was previously described. The computed flutter dynamic pressure and frequency were determined by interpolating the specified dynamic pressures and the computed frequencies to the zero damping value of the flutter mode. The flutter mode for all freestream Mach numbers considered in this study was dominated by motion in the first bending mode. A summary of the computed flutter characteristics in terms of flutter speed index $\frac{U_f}{b\omega_\alpha\sqrt{\mu}}$ and nondimensional flutter frequency ratio $\frac{\omega}{\omega_\alpha}$ is shown in Table 1. For M_∞ = 0.9, Ref. 3 reports a computed flutter speed index of 0.353 and a computed flutter frequency ratio of 0.42. These results agree very well with those shown in Table 1 for M_∞ = 0.9 which verifies the addition of the structural equations of motion to CFL3D version 2.1.

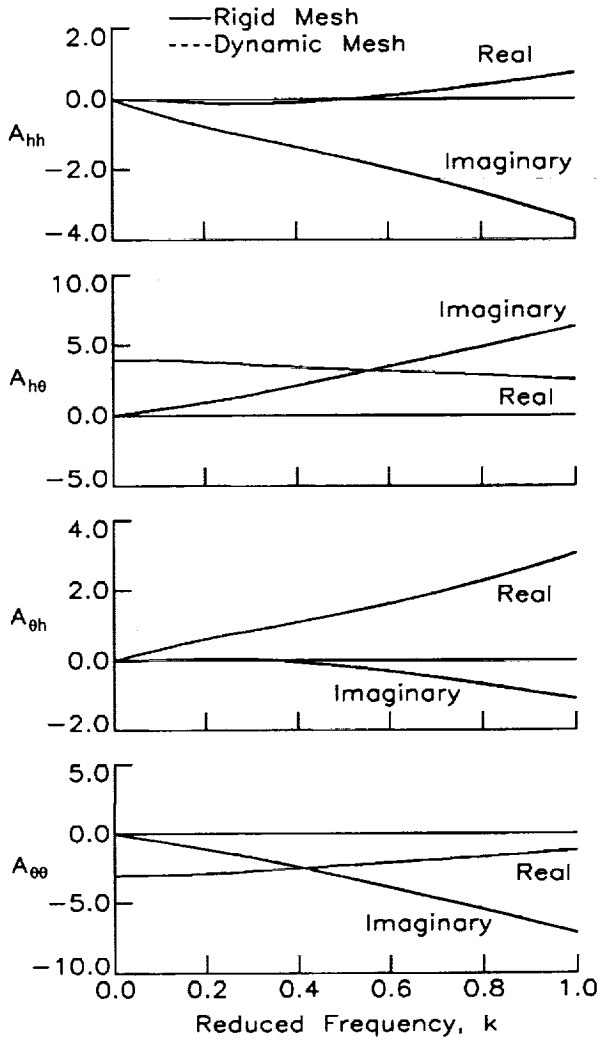

Figure 5 Comparison of generalized aerodynamic forces for the rigid pitch and plunge of Wing 445.6 at M_∞ = 0.9 and $\alpha = 0°$.

Table 1 Summary of computed flutter results for Wing 445.6.

M_∞	Flutter Speed Index	Flutter Frequency Ratio
0.499	0.439	0.597
0.678	0.417	0.539
0.900	0.352	0.425
0.960	0.275	0.343
0.990	0.310	0.373
1.072	0.466	0.541
1.141	0.660	0.764

The computed flutter characteristics are compared with the experimentally measured values of flutter speed index and flutter frequency ratio in Fig. 6. The experimental data defines a typical transonic flutter "dip" with the bottom near M_∞ = 1.0. At the subsonic freestream Mach numbers (M_∞ = 0.499 and 0.678), the computed flutter speed indexes agree well with the experimental values while the computed frequency ratios are slightly larger than the experimental values. It is interesting to note that at these subsonic freestream Mach numbers the computed flutter results are characterized by "hard" flutter crossings. In other words, small changes in dynamic pressure result in large changes in the damping of the flutter mode. At M_∞ = 0.9 and 0.96, the computed flutter speed indexes are less than the experimental values and the frequency ratios agree well with the experimental values. The computed flutter results at these freestream Mach numbers are characterized by a "mild" flutter crossing. Although there was no experimental flutter point determined at M_∞ = 0.99, computational results are included to aid in identifying the bottom of the flutter "dip". The computational results at M_∞ = 0.99 are compared in Fig. 6 to estimated values of flutter speed and frequency determined from the faired curves in Fig. 16 of Ref. 23. These faired curves which were based on the experimentally determined flutter points, the experimentally determined no-flutter track, and analytic calculations are considered to be of reasonable accuracy.[24] The computational results at M_∞ = 0.99 as well as those at M_∞ = 1.072 and 1.141 indicate a premature rise in the computational flutter boundary as compared with the experimental boundary. Although the boundary is more sensitive to freestream Mach number in this range, the computed flutter results are still characterized by a "mild" flutter crossing.

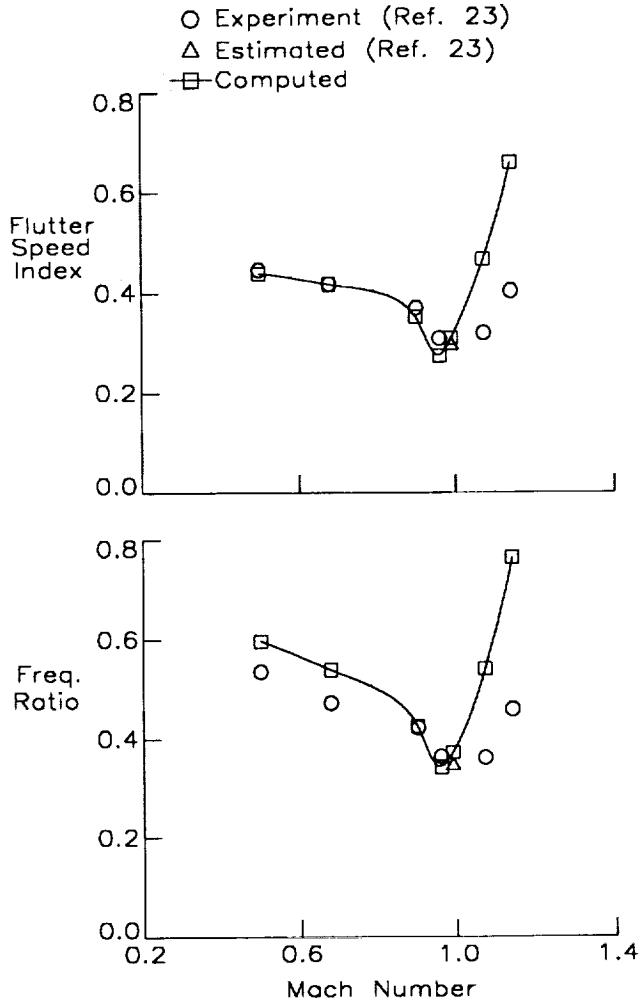

Figure 6 Comparison of Euler flutter predictions with experimental data for Wing 445.6.

Computational results for this configuration obtained with linear theory and TSD methods were previously reported in Ref. 16. In this report, three sets of flutter results were presented: results from a linear theory subsonic kernel-function program, results using the linear potential equation and modeling the wing aerodynamically as a flat plate, and results using the complete (nonlinear) TSD equation and including wing thickness. Flutter results, flutter speed index and flutter frequency, from the subsonic kernel-function and the potential equation compare well with the experimental data over the range of freestream Mach numbers from 0.338 to 1.141. (Note that the subsonic kernel-function results are limited to the subsonic freestream Mach numbers.) Results from the nonlinear TSD equation for the subsonic freestream Mach numbers 0.678, 0.901, and 0.96 indicate that the flutter speed index is decreased by 1%, 5%, and 19%, respectively, from the experimental results with a similar decrease in the flutter frequency. These results are similar to the trend shown by the current computations in Fig. 6. Subsequent unpublished calculations by the authors of Ref. 16 indicate that flutter results for the supersonic freestream Mach numbers which were obtained with the nonlinear TSD equation are highly non-conservative. This trend is also consistent with the results shown in Fig. 6. It is counter-intuitive that the higher-order methods utilizing the TSD and Euler equations should produce flutter results which compare less favorably with the experimental results than with the results based on linear methods. However, it is important to note that the modeling of the flow physics is incomplete even when using the TSD and Euler equations. The existence and effect of highly nonlinear flow phenomena such as strong shocks and viscous boundary layers must be investigated before any conclusions can be drawn.

Steady-state Mach contours of the initial flowfields on the upper wing surface are shown in Figs. 7(a)-7(d) to illustrate the basic flow characteristics at the selected freestream Mach numbers of 0.96, 0.99, 1.072, and 1.141 where time-marching flutter calculations were made. Mach contours for M_∞ = 0.400, 0.678, and 0.900, which are not shown, indicate a smooth expansion and recompression of the flow from the leading edge to the trailing edge with very little variation in the spanwise direction and no supercritical flow. Mach

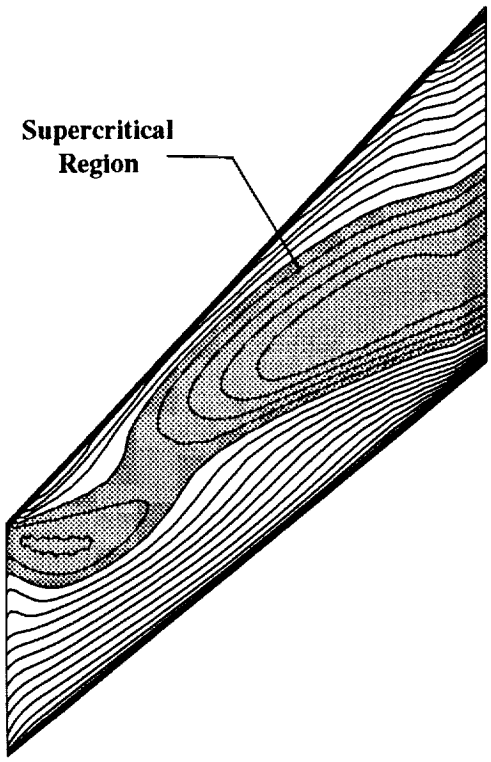

(a) $M_\infty = 0.96$.

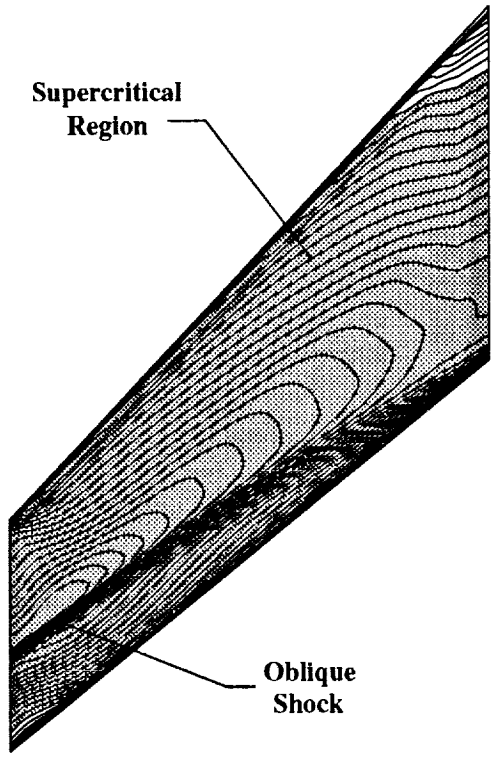

(c) $M_\infty = 1.072$.

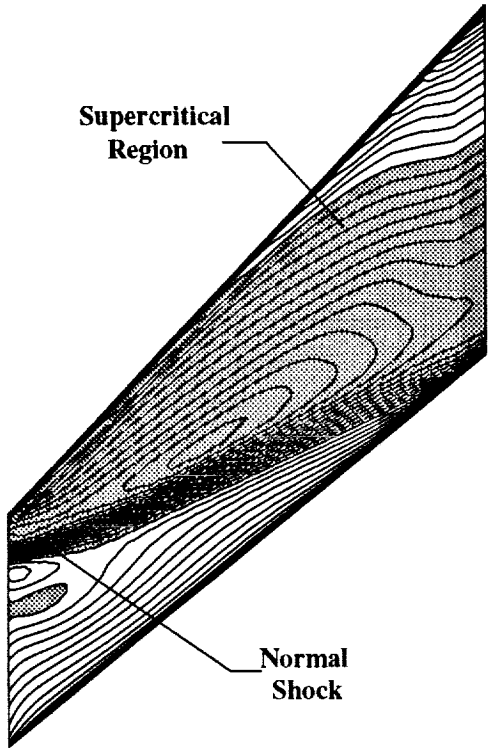

(b) $M_\infty = 0.99$.

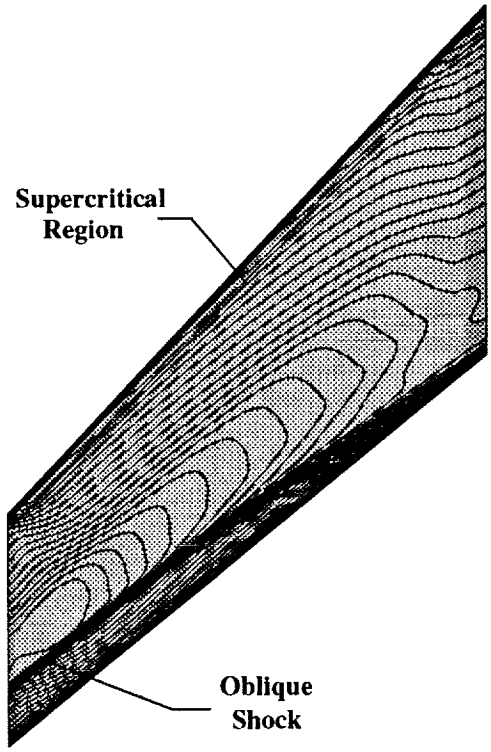

(d) $M_\infty = 1.141$.

Figure 7 Comparison of steady-state Mach contours on the upper surface of Wing 445.6.

Figure 7 Concluded.

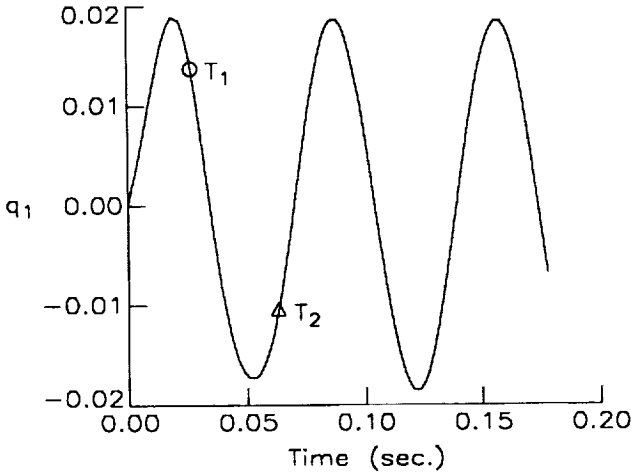

Figure 8 Time history of the first generalized displacement for the Wing 445.6 at $M_\infty = 0.99$ and $\alpha = 0°$.

contours shown in Fig. 7(a) indicate that at $M_\infty = 0.96$ an area of supercritical flow has formed on the wing. This area of supercritical flow does not terminate with a shock. Figure 7(b) shows that at $M_\infty = 0.99$ the areas of supercritical flow has expanded, and a normal shock has formed near the tip of the wing at approximately 25% of the local chord. Mach contours for $M_\infty = 1.702$ and 1.141, shown in Figs. 7(c) and 7(d), respectively, indicate that with further increases in freestream Mach number, the normal shock transitions to an oblique shock located further downstream on the outboard portion of the wing at approximately 70% of the local chord. Also, at $M_\infty = 1.141$, the spanwise extent of the oblique shock has increased to approximately 50% of the outboard portion of the wing. Rapid changes in the steady-state flow conditions from $M_\infty = 0.96$ to 1.141 are indicated by the formation and movement of a shock at the tip of the wing. This range of freestream Mach number also corresponds to the range of Mach numbers where the computed flutter boundary rapidly rises (See Fig. 6). Therefore, small variations due to errors associated with modeling deficiencies and computational deviations could be expected to have a large effect on the final flutter speed and frequency. Modeling deficiencies could be due to the neglect of the viscous effects. Computationally, these errors might be due to a lack of spatial convergence.

The rapid changes in the steady-state flowfield conditions from $M_\infty = 0.96$ to 1.141 suggest that, for a given freestream Mach number in this range, the flow characteristics can also change rapidly during an aeroelastic transient. Figure 8 shows the time history of the first generalized displacement q_1 for a time-marching aeroelastic transient at $M_\infty = 0.99$ and at a freestream dynamic pressure of 1.12 times the estimated experimental value. Recall that q_1 corresponds to the first bending mode which is the dominant component of the flutter mode. The damping and frequency content of this aeroelastic transient indicates that the wing is dynamically unstable at this condition. Instantaneous surface contours of the pressure coefficient C_p are shown in Figs. 9 and 10 for the times T_1 and T_2, respectively, which are indicated in Fig. 8. Upper and lower surface pressures are shown at these points in time with $\Delta C_p = 0.02$. At T_1, contours on the upper surface indicate that an upper surface shock has disappeared while contours on the lower surface indicate that a lower surface shock has strengthened and moved slightly downstream. Similarly, at T_2, the opposite has occurred. The shock has weakened on the lower surface and strengthened on the upper surface. Figures 9 and 10 therefore show that during the aeroelastic transient, rapid changes in surface pressures occur due to the formation and disappearance of a normal shock on the tip of the wing. Figures 9 and 10 also illustrate an unusual shock behavior during the aeroelastic transient in that there is little chordwise movement of the shock as it strengthens and weakens. For two-dimensional airfoils, significant shock weakening is usually accompanied by large shock motion.

Conclusions

Modifications to an existing three-dimensional, implicit, upwind Euler/Navier-Stokes code (CFL3D Version 2.1) for the aeroelastic analysis of wings was described. These modifications included the incorporation of a deforming mesh algorithm and the addition of the structural equations of motion for their simultaneous time-integration with the governing flow equations. Euler results from calculations performed for a rigid wing undergoing forced pitching and plunging motions were presented to check the deforming mesh algorithm. Aeroelastic Euler results for a 45° swept-back wing at a freestream Mach number of 0.9 were compared to those presented in Ref. 3 to check the addition of the structural equations of motion. Calculated flutter results for the same 45° swept-back wing were compared with the experimental data for seven freestream Mach numbers which define the flutter boundary over a range of Mach number from 0.499 to 1.14. These comparisons showed good agreement in flutter characteristics for freestream Mach numbers below unity. For freestream Mach numbers above unity, the computed aeroelastic results predicted a premature rise in the flutter boundary as compared with the experimental boundary. Steady-state Mach contours of the initial flowfields illustrated rapid changes in the basic flow characteristics from $M_\infty = 0.96$ to 1.141 which is indicated by the formation and movement of a shock near the tip of the wing. Instantaneous surface pressure contours during an aeroelastic transient at $M_\infty = 0.99$ also demonstrated significant changes in the flowfield due to the formation and disappearance of a normal shock on the tip of the wing which is induced by the aeroelastic motions at this freestream Mach number.

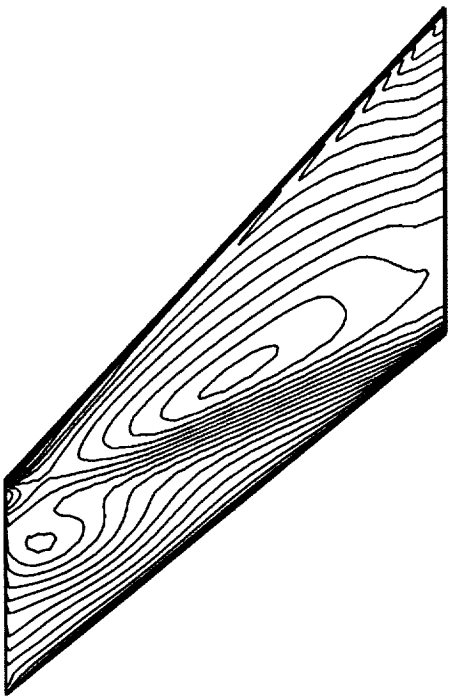

(a) upper surface.

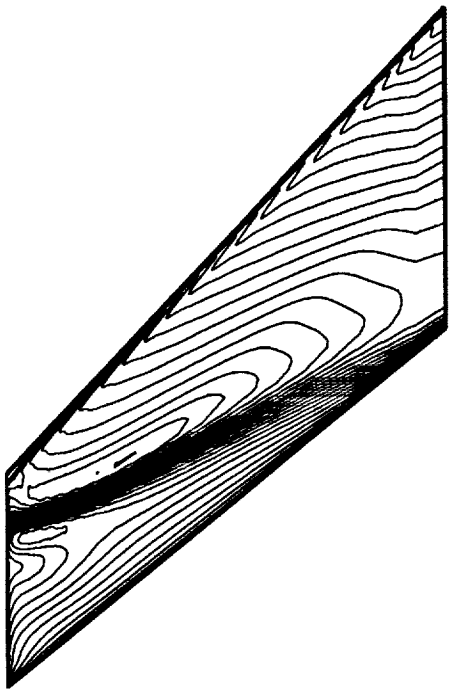

(b) lower surface.

Figure 9 Instantaneous surface contours of the pressure coefficient at time T_1 for the Wing 445.6 at $M_\infty = 0.99$ and $\alpha = 0°$.

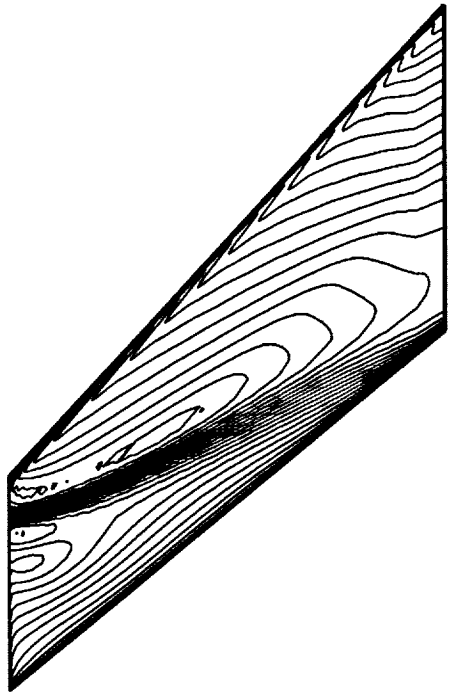

(a) upper surface.

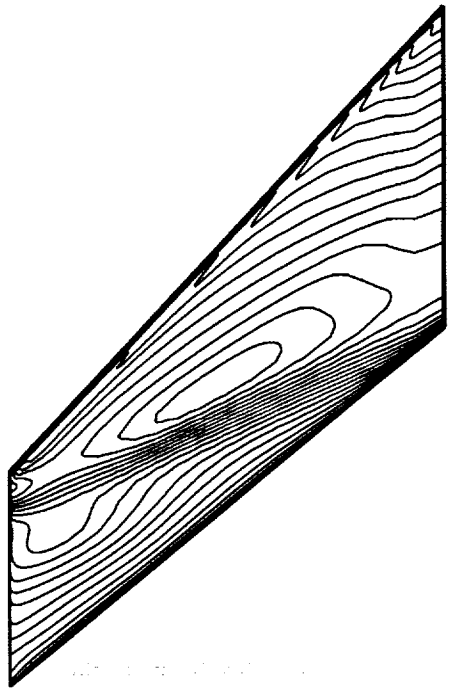

(b) lower surface.

Figure 10 Instantaneous surface contours of the pressure coefficient at time T_2 for the Wing 445.6 at $M_\infty = 0.99$ and $\alpha = 0°$.

Acknowledgments

The authors would like to thank Brian A. Robinson of McDonnell Aircraft Company, St. Louis, Missouri, for providing the computational grid and for sharing his experiences concerning the aeroelastic version of CFL3D. The authors would also like to thank James L. Thomas, W. Kyle Anderson and Christopher L. Rumsey of the Computational Aerodynamics Branch, NASA Langley Research Center, and Sherrie L. Krist of ViGYAN Inc., Hampton, Virginia, for their many helpful discussions concerning CFL3D. Finally, the authors would like to thank their colleague, Robert M. Bennett, for sharing his many insights into computational aeroelasticity and flutter.

References

[1] Edwards, J. W.; and Malone, J. B., "Current Status of Computational Methods for Unsteady Transonic Unsteady Aerodynamics and Aeroelastic Analysis," Presented at the AGARD Structures and Materials Panel Specialist's Meeting on Transonic Unsteady Aerodynamics and Aeroelasticity, Paper No. 1, October 1991.

[2] Guruswamy, G. P., "Time-Accurate Unsteady Aerodynamic and Aeroelastic Calculations of Wings Using Euler Equations," AIAA Paper No. 88-2281, April 1988.

[3] Robinson, B. A.; Batina, J. T.; and Yang, H. T. Y., "Aeroelastic Analysis of Wings Using the Euler Equations with a Deforming Mesh," *Journal of Aircraft*, vol. 28, pp. 778–788, November 1991.

[4] Schuster, D.; Vadyak, J.; and Atta, E., "Static Aeroelastic Analysis of Fighter Aircraft Using a Three-Dimensional Navier-Stokes Algorithm," AIAA Paper No. 90-0435, January 1990.

[5] Guruswamy, G. P., "Numerical Simulation of Vortical Flows on Flexible Wings," AIAA Paper No. 89-0537, January 1989.

[6] Guruswamy, G. P., "Vortical Flow Computations on Swept Flexible Wings Using Navier-Stokes Equations," AIAA Paper No. 89-1183, April 1989.

[7] Guruswamy, G. P., "Navier-Stokes Computations on Swept-Tapered Wings, Including Flexibility," AIAA Paper No. 90-1152, April 1990.

[8] Guruswamy, G. P., "Vortical Flow Computations on a Flexible Blended Wing-Body Configuration," AIAA Paper No. 91-1013-CP, April 1991.

[9] Obayashi, S.; Guruswamy, G. P.; and Goorjian, P., "Application of a Streamwise Upwind Algorithm for Unsteady Transonic Computations Over Oscillating Wings," AIAA Paper No. 90-3103, August 1990.

[10] Obayashi, S.; and Guruswamy, G. P., "Unsteady Shock-Vortex Interaction on a Flexible Delta Wing," AIAA Paper No. 91-1109, April 1991.

[11] Rausch, R. D.; Batina, J. T.; and Yang, H. T. Y., "Three-Dimensional Time-Marching Aeroelastic Analyses Using An Unstructured-Grid Euler Method ," AIAA Paper No. 92-2506, April 1992.

[12] Yates, E. C., Jr., "AGARD Standard Aeroelastic Configuration for Dynamic Response, Candidate Configuration I.-Wing 445.6," NASA TM 100492, August 1987.

[13] Anderson, W. K.; Thomas, J. L.; and van Leer, B., "Comparison of Finite Volume Flux Vector Splitting for the Euler Equations," *AIAA Journal*, vol. 24, no. 9, pp. 1435–1460, 1986.

[14] Anderson, W. K.; Thomas, J. L.; and Rumsey, C. L., "Extension and Applications of Flux-Vector Splitting to Unsteady Calculations on Dynamic Meshes," AIAA Paper No. 87-1152, June 1987.

[15] Batina, J. T., "Unsteady Euler Algorithm With Unstructured Dynamic Mesh for Complex-Aircraft Aeroelastic Analysis," AIAA Paper No. 89-1189, April 1989.

[16] Cunningham, H. J.; Batina, J. T.; and Bennett, R. M., "Modern Wing Flutter Analysis by Computational Fluid Dynamics Methods," *Journal of Aircraft*, vol. 25, no. 10, pp. 962–968, 1988.

[17] Edwards, J. W.; Bennett, R. M.; Whitlow, W., Jr; and Seidel, D. A., "Time-Marching Transonic Flutter Solutions Including Angle-of-Attack Effects," AIAA Paper No. 82-3685, May 1982.

[18] Edwards, J. W.; Bennett, R. M.; Whitlow, W., Jr; and Seidel, D. A., "Time-Marching Transonic Flutter Solutions Including Angle-of-Attack Effects," *Journal of Aircraft*, vol. 20, no. 11, pp. 899–906, 1984.

[19] Bennett, R. M.; and Desmarais, R. N., "Curve Fitting of Aeroelastic Transient Response Data with Exponential Functions," Flutter Testing Techniques NASA SP-415, May 1975.

[20] Seidel, D. A.; Bennett, R. M.; and Whitlow, W. W., "An Exploratory Study of Finite Difference Grids for Transonic Unsteady Aerodynamics," AIAA Paper No. 83-0503, January 1983.

[21] Seidel, D. A.; Bennett, R. M.; and Ricketts, R. H., "Some Recent Applications of XTRAN3S," AIAA Paper No. 83-1811, July 1983.

[22] Rausch, R. D.; Batina, J. T.; and Yang, H. T. Y., "Euler Flutter Analysis of Airfoils Using Unstructured Dynamic Meshes," *Journal of Aircraft*, vol. 27, no. 5, pp. 436–443, 1990.

[23] Yates, E. C., Jr.; Land, N. S.; and Foughner, J. T., Jr., "Measured and Calculated Subsonic and Transonic Flutter Characteristics of a 45 deg Sweptback Wing Planform in Air and in Freon-12 in the Langley Transonic Dynamics Tunnel," NASA TN D-1616, March 1963.

[24] Yates, E. C., Jr., "Private Communication." July 1992.

REPORT DOCUMENTATION PAGE

Form Approved
OMB No. 0704-0188

1. AGENCY USE ONLY (Leave blank)	2. REPORT DATE	3. REPORT TYPE AND DATES COVERED
	March 1993	Technical Memorandum

4. TITLE AND SUBTITLE
Wing Flutter Boundary Prediction Using an Unsteady Euler Aerodynamic Method

5. FUNDING NUMBERS
505-63-50-12

6. AUTHOR(S)
Elizabeth M. Lee-Rausch
John T. Batina

7. PERFORMING ORGANIZATION NAME(S) AND ADDRESS(ES)
NASA Langley Research Center
Hampton, VA 23681-0001

8. PERFORMING ORGANIZATION REPORT NUMBER

9. SPONSORING / MONITORING AGENCY NAME(S) AND ADDRESS(ES)
National Aeronautics and Space Administration
Washington DC 20546-0001

10. SPONSORING / MONITORING AGENCY REPORT NUMBER
NASA TM 107732

11. SUPPLEMENTARY NOTES
Paper will be presented at the 34th AIAA/ASME/ASCE/AHS/ASC Structures, Structural Dynamics and Materials Conference, La Jolla, California, April 1993.

12a. DISTRIBUTION / AVAILABILITY STATEMENT
Unclassified - Unlimited
subject Category 02

12b. DISTRIBUTION CODE

13. ABSTRACT *(Maximum 200 words)*

Modifications to an existing three-dimensional, implicit, upwind Euler/Navier-Stokes code (CFL3D Version 2.1) for the aeroelastic analysis of wings are described. These modifications, which were previously added to CFL3D Version 1.0, include the incorporation of a deforming mesh algorithm and the addition of the structural equations of motion for their simultaneous time-integration with the governing flow equations. The paper gives a brief description of these modifications and presents unsteady calculations which check the modifications to the code. Euler flutter results for an isolated 45° swept-back wing are compared with experimental data for seven freestream Mach numbers which define the flutter boundary over a range of Mach number from 0.499 to 1.14. These comparisons show good agreement in flutter characteristics for freestream Mach numbers below unity. For freestream Mach numbers above unity, the computed aeroelastic results predict a premature rise in the flutter boundary as compared with the experimental boundary. Steady and unsteady contours of surface Mach number and pressure are included to illustrate the basic flow characteristics of the time-marching flutter calculations and to aid in identifying possible causes for the premature rise in the computational flutter boundary.

14. SUBJECT TERMS
Aeroelasticity
Unsteady Aerodynamics
Transonic Aerodynamics
Computational Fluid Dynamics

15. NUMBER OF PAGES
12

16. PRICE CODE
A03

17. SECURITY CLASSIFICATION OF REPORT	18. SECURITY CLASSIFICATION OF THIS PAGE	19. SECURITY CLASSIFICATION OF ABSTRACT	20. LIMITATION OF ABSTRACT
Unclassified	Unclassified	Unclassified	